JOURNAL OF GEOPHYSICAL RESEARCH, VOL. 103, NO. B9, PAGES 21,299–21,314, SEPTEMBER 10, 1998

Geometry and mechanics of secondary fracturing around small three-dimensional faults in granitic rock

Stephen J. Martel and William A. Boger

Department of Geology and Geophysics, University of Hawaii, Honolulu

Abstract. The orientations, locations, sizes, and relative abundances of secondary fractures observed along small natural faults can be accounted for by a three-dimensional elastic model. Secondary fractures along small subvertical left-lateral strike-slip faults in massive granitic rock of the Sierra Nevada of California (1) consistently strike 25°±10° counterclockwise from their host faults and dip at angles greater than 80°; (2) generally are absent along the central portions of the fault traces; (3) are numerous near the ends of some fault traces but absent along others; and (4) in rare cases form echelon arrays either centered along a fault trace or just past the fault trace ends. These observations are consistent with secondary fractures that nucleated near the perimeter of an elliptical fault along a "cohesive rim" of high slip resistance and propagated in three dimensions normal to the local most tensile stress. The fracture orientations relative to the faults reflect small stress drops during slip on the faults. The observations and model together have direct implications for how faults grow and conduct fluids. Secondary fractures are likely to be larger at the ends of small strike-slip faults rather than at their tops and bottoms. As a result, if strike-slip faults grow in an unrestricted manner, they are more likely to be linked end-to-end rather than top-to-bottom, especially where slip is small. Hydraulic conductivity is likely to be enhanced at the linkages between faults, so highly conductive regions along linked strike-slip faults are more likely to be vertical rather than horizontal.

1. Introduction

A recent report by the *National Academy of Sciences* [1996] on the flow of fluids along fractures in rock noted that three key questions commonly arise in scientific and engineering investigations of fractured rock:

1. How can the fractures that are significant hydraulic conductors be identified, located, and characterized?
2. How do fluid and chemical transport occur in fracture systems?
3. How can changes to fracture systems be predicted and controlled?

The report concluded that knowledge of the processes responsible for producing distinctive fracture patterns can help us understand systems of fracture flow, and in particular, that understanding the geometry of fracture systems in the field is a central issue. This paper addresses these points.

The specific focus here is on the effect of secondary fractures along faults, fractures that form in response to fault slip. These fractures can link originally discontinuous faults both mechanically [*Segall and Pollard,* 1983; *Martel,* 1990; *Bürgmann et al.,* 1994] and hydraulically [*Long and Witherspoon,* 1985; *National Academy of Sciences,* 1996]. As a result, secondary fractures must greatly influence how faults grow and how fluids circulate in the Earth's crust.

Explanations for these fractures should be physically plausible and consistent with field observations. The occurrence of secondary fractures near fault trace ends is in general consistent with the strong stress concentrations predicted there by linear elastic fracture mechanics, or LEFM [*Erdogan and Sih,* 1963; *Pollard and Segall,* 1987]. In conventional LEFM treatments, however, a physically implausible stress singularity is predicted at the tip (two-dimensional (2-D)) or perimeter (three-dimensional (3-D)) of a fracture [e.g., *Lawn and Wilshaw,* 1975; *Kassir and Sih,* 1975]. In cohesive zone theory, or CZT [e.g., *Dugdale,* 1960; *Barenblatt,* 1962; *Rudnicki,* 1980; *Martel,* 1997], this singularity is eliminated by postulating an enhanced resistance to slip near the fault trace end in a "cohesive zone." The resisting cohesive zone shear stresses annul the stress singularity that otherwise would arise at the fault trace end. A series of recent papers have applied CZT to address slip and deformation along faults [*Martel and Pollard,* 1989; *Cowie and Scholz,* 1992; *Bürgmann et al.,* 1994; *Willemse et al.,* 1996; *Cooke,* 1997; *Willemse,* 1997; *Martel,* 1997]. *Willemse* [1997] provided the only three-dimensional treatment of cohesive zones in the context of faulting, but he did not focus on secondary fracturing.

In addition to these mechanically based models, several investigators have produced secondary fractures around three-dimensional shear fractures in blocks of plastic in laboratory tests [*Adams and Sines,* 1978; *Germanovich et al.,* 1994; *Cooke and Pollard,* 1996]. Shear fractures in the plastics develop without the grain-scale influences in rock samples [e.g., *Peng and Johnson,* 1972; *Tapponier and Brace,* 1976; *Wong,* 1982] and thus are appropriate to consider in an examination of faults with dimensions of several meters or more. Other than a brief discussion by *Scholz* [1990], the conceptual three-dimensional models arising from laboratory studies have not been rigorously compared to secondary fractures along natural faults in the earth.

This paper opens by describing patterns of secondary fractures along small faults in the Sierra Nevada of California. These observations are used to construct a geometric model of fracturing around a simple three-dimensional fault. Three-dimensional

Copyright 1998 by the American Geophysical Union.

Paper number 98JB01393.
0148-0227/98/98JB-01393$09.00

LEFM and CZT mechanical models are discussed next and examined in light of the field observations and then are compared to the conceptual models and the laboratory results of other investigators. The paper concludes with a discussion of applications for three-dimensional cohesive zone models.

2. Field Observations

2.1. Small Faults

Small faults and joints of the Sierra Nevada batholith are well-suited for field investigation owing to their abundance and superb exposures. The most detailed observations have been made in the drainage of Bear Creek [*Segall and Pollard,* 1980, 1983; *Segall and Simpson,* 1986; *Martel et al.,* 1988; *Martel,* 1990; *Bürgmann and Pollard,* 1994; *Christiansen,* 1995] in the Mount Abbot 15' quadrangle, but faults and joints throughout the batholith have a similar appearance [e.g., *Moore,* 1963; *Lockwood and Moore,* 1979]. Radiometric analyses indicate the faulting at Bear Creek occurred between 72 Ma and 75-79 Ma [*Segall et al.,* 1990]. Geochemical, mineralogical, and microstructural evidence suggest that during faulting the ambient pressure was about 100-200 MPa and the temperature was ~300-350°C [*Martel et al.,* 1988; *Ague and Brimhall,* 1988]. These conditions most likely reflect a depth of faulting of several kilometers.

The predominant joints and small faults of Bear Creek strike east-northeast, dip steeper than 80°, and are less than a centimeter thick. Their traces typically are straight and less than several tens of meters long. Based on their straight trace geometries on surfaces of varied orientations, the joints and small faults can be idealized as planar features. The joints are mineralized, containing undeformed crystals of chlorite and epidote. The faults also are mineralized but contain deformed mineral assemblages of chlorite and epidote ± quartz ± calcite ± white mica [*Segall et al.,* 1990]. The abundance of quartz along many faults is striking given how scarce quartz is along the joints; this key point will be pursued further in the discussion. The faults display subhorizontal slickenlines, and they offset dikes and inclusions left-laterally. The faults thus appear to be nearly pure left-lateral strike-slip faults. *Segall and Pollard* [1983] argued compellingly that the small faults did not originate as shear fractures but rather from shearing of preexisting joints. This shearing presumably reflects changes in the orientations of the regional principal stresses after the joints opened.

2.2. Secondary Fractures

Secondary fractures developed along many of the small faults [*Moore,* 1963; *Segall and Pollard,* 1980, 1983; *Bürgmann and Pollard,* 1994; *Martel,* 1997]. In numerous cases they link originally discontinuous faults together. Secondary fractures can be grouped according to how their traces are distributed along a fault trace.

2.2.1. Secondary fracture traces that intersect fault trace ends. Traces of secondary fractures most commonly occur near but behind the ends of a small fault trace (Figure 1), and they are rare away from fault trace ends. The secondary fractures usually dip steeper than 80°, have gently curved traces, and strike 25°±10° counterclockwise from the faults; fracture strikes outside this range are remarkably rare. The fractures appear planar in three-dimensional exposures, not twisted. The secondary fractures are not symmetrically arranged along the faults. Near, but behind an end of a fault trace, secondary fractures occur only on one side of the fault. Near the east-northeast end of a fault trace secondary fractures extend only to the northeast, whereas near the west-southwest end of a fault trace the secondary fractures extend only to the southwest. Significantly, secondary fractures do not occur near the ends of all fault traces, and along some fault traces several secondary fractures exist. The trace length of a secondary fracture typically does not exceed a few percent of the trace length of the host fault. Where secondary fractures cut inclusions, the margins of the inclusions are aligned, indicating that the secondary fractures originated as opening mode fractures and not shear fractures. Although most secondary fractures have exposed thicknesses of no more than a few millimeters, some have apertures of several centimeters and are filled with quartz, chlorite, and epidote. Usually, no more than a few secondary fractures occur near the end of a fault trace (e.g., Figure 1); commonly, there is one or none.

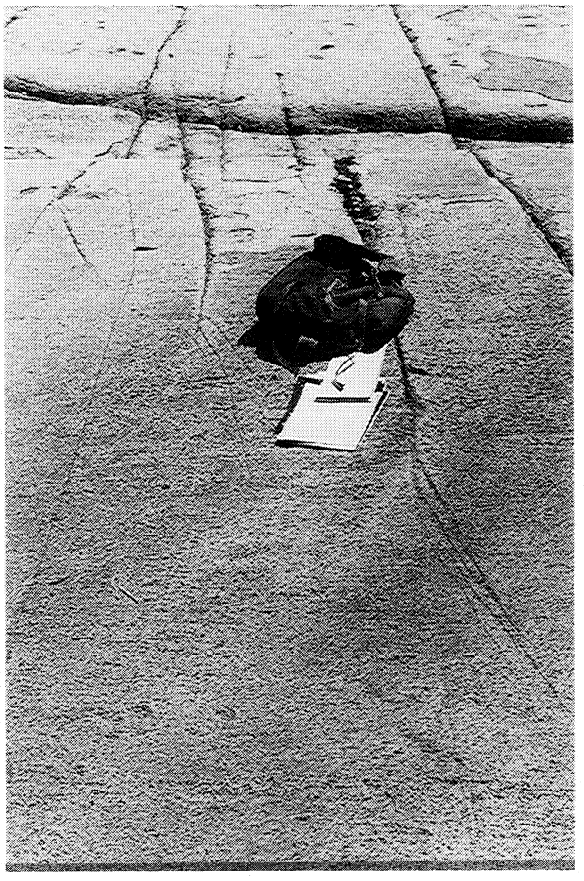

Figure 1. Photograph showing oblique secondary fractures near the end of a small fault. Photograph taken at the Kip Camp outcrop of *Segall and Pollard* [1983], where faults strike approximately N65°E on average.

2.2.2 Secondary fracture traces past fault trace ends. Secondary fracture traces locally occur past fault trace ends (Figure 2). These extend across the projection of the fault trace in contrast to the more common secondary fractures that intersect a fault trace near its end. These secondary fractures generally strike 25°±10° counterclockwise relative to the fault and appear to dip about as steeply as the fault. Fracture patterns such as this are not unique to the faults of Bear Creek: *Granier* [1985] and *Martel and Peterson* [1991] have documented similar fracture arrays near the ends of faults in Europe.

2.2.3. Bands of echelon secondary fractures. Parallel to some faults are structures several meters long that contain

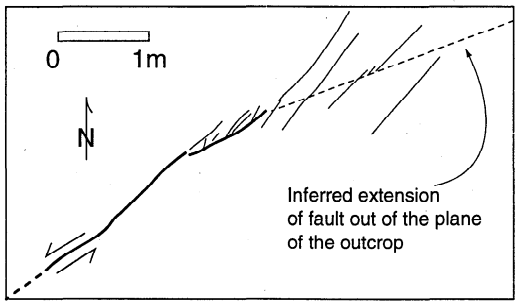

Figure 2. Secondary fractures (light lines) past the northeast end of a fault trace (heavy line). The southwest end of the fault (heavy dashed line) is concealed. The inferred extension of the fault out of the plane of the outcrop is shown in a light dashed line. This fault is located about 200 m north of the Waterfall site of *Martel* [1990]. The local strike of the fault ranges from N50°E to N70°E.

numerous echelon fractures with trace lengths less than several centimeters (Figure 3). We informally refer to these structures as "zipper crack bands." The short fractures forming a band typically dip steeper than 80° and generally strike 25°±10° counterclockwise from the strike of the band as a whole. The fractures appear to be planar, not twisted. They are mineralized with epidote and chlorite. Along some bands, no central fracture is exposed (Figure 3a), but along others, a fracture a few millimeters thick containing epidote and chlorite extends along the center of the band (Figure 3b). Where a central filling is present, the secondary fracture traces extend about equal distances on either side of the filling trace. We have not been able to measure any slip across the central fractures of zipper crack bands; if slip has occurred, it is less than a millimeter or so. In spite of careful field inspection, we also have been unable to determine whether the short oblique fractures cut the central fracture or vice-versa. Zipper crack bands are far less common than secondary fractures that intersect a fault trace near its end.

3. Conceptual Geometric Model

Figure 4 shows a conceptual three-dimensional geometric model, based on the Sierran field observations, of a small vertical left-lateral fault with secondary fractures. Figure 4 shows the south face of the fault as viewed from the southwest. In the attendant coordinate system the z axis is horizontal and points south, normal to the fault. The x axis points east, and the y axis points up. A horizontal plane through the fault center (e.g., plane C of Figure 4) intersects the fault in a line we term the equator.

We postulate that the small faults are elliptical. The traces of the faults of Bear Creek do not require an elliptical fault geometry, but such a geometry is consistent with the surface textures widely observed on joints in massive rock [e.g., *Pollard and Aydin,* 1988], and the simple faults of Bear Creek originated as joints [*Segall and Pollard,* 1983]. Simple normal faults (i.e., single faults with a planar slip surface) in sedimentary rocks also have been inferred to have roughly elliptical shapes based on their slip distributions [*Barnett et al.,* 1987; *Walsh and Watterson,* 1989; *Nicol et al.,* 1996]. In our geometric model (Figure 4) we show the simplest elliptical form, that of a penny.

Secondary fractures in Figure 4 are depicted as vertical and planar, and they are centered near the perimeter of the fault. We envision three general shapes of secondary fractures. Each shape can be formed from one or two semicircles. Semicircular (i.e., D-shaped) fractures do not extend across the fault. P-shaped fractures extend past the fault perimeter, flare out to cross the fault plane, and then extend down the other side a small distance. Circular (i.e., O-shaped) fractures are the third shape. Depending on one's perspective and where one looks around the fault perimeter, the P- and D-shaped secondary fractures can appear backward or upside-down.

In describing the location of fractures around our conceptual penny-shaped strike-slip fault, we adopt a "clock-face" convention. The 12:00 and 6:00 positions refer to the top and bottom of the fault, respectively; a line in the plane of the fault that is tangent to the fault perimeter is horizontal at those points. The 3:00 and 9:00 positions refer to the west and east ends of the fault, respectively; a line tangent to the fault perimeter is vertical there.

The geometric model accounts for each of the three secondary fracture distributions previously described. A horizontal cross section through the fault center (plane C of Figure 4) yields the most commonly observed fracture trace distribution, that of secondary fractures (if present) being concentrated near the end of a fault trace. The secondary fractures intersected by plane C are D-shaped. A horizontal cross section through the 1:30 position (plane B of Figure 4) can yield secondary fractures that intersect the fault trace as well as fracture traces that occur past the tip of a fault trace. In order to produce the pattern of Figure 2, where secondary fracture traces extend across the projection of a fault trace, the secondary fractures must extend past the fault perimeter and across to the other side (i.e., be P-shaped). Horizontal cross sections near the 12:00 or 6:00 positions can yield the zipper crack arrays. The fractures intersected here are O-shaped and extend the same distance on either side of the fault. A slice just above the fault top (plane A of Figure 4) would reveal only a zipper crack band. A slice just above the bottom of the fault (plane D of Figure 4) would yield a zipper crack band along with a central fracture (the fault) provided that the secondary fractures can grow a small distance vertically back toward the fault center (i.e., be O-shaped).

If the conceptual geometric model is valid, it indicates how the secondary fractures grow. First, the notable scarcity of secondary fractures along the central portion of most fault traces (e.g., Figure 1) and the scarcity of zipper crack bands with central fractures require that secondary fractures do not propagate vertically for a significant fraction of a fault radius back toward the fault equator. Second, examples of secondary fractures past fault trace tips (Figure 2) are scarce, as are fault-parallel zipper crack bands that lack central fractures. This suggests that secondary fractures do not propagate vertically for a significant fraction of a fault radius away from the fault equator. Third, secondary fractures like those in the zipper crack band of Figure 3b must have either propagated through the fault or else propagated vertically past the fault perimeter and then propagated back toward the fault center on the other side of the fault (i.e., be O-shaped).

4. Mechanical Models

Mechanical models for secondary fracturing around three-dimensional faults can be based on either LEFM or CZT. We first discuss an LEFM model and how it corresponds to our field observations and conceptual geometric model, and then we explore a CZT model. The key aspects of secondary fracturing that we seek to account for are the locations, orientations, relative sizes, and relative abundances of the fractures.

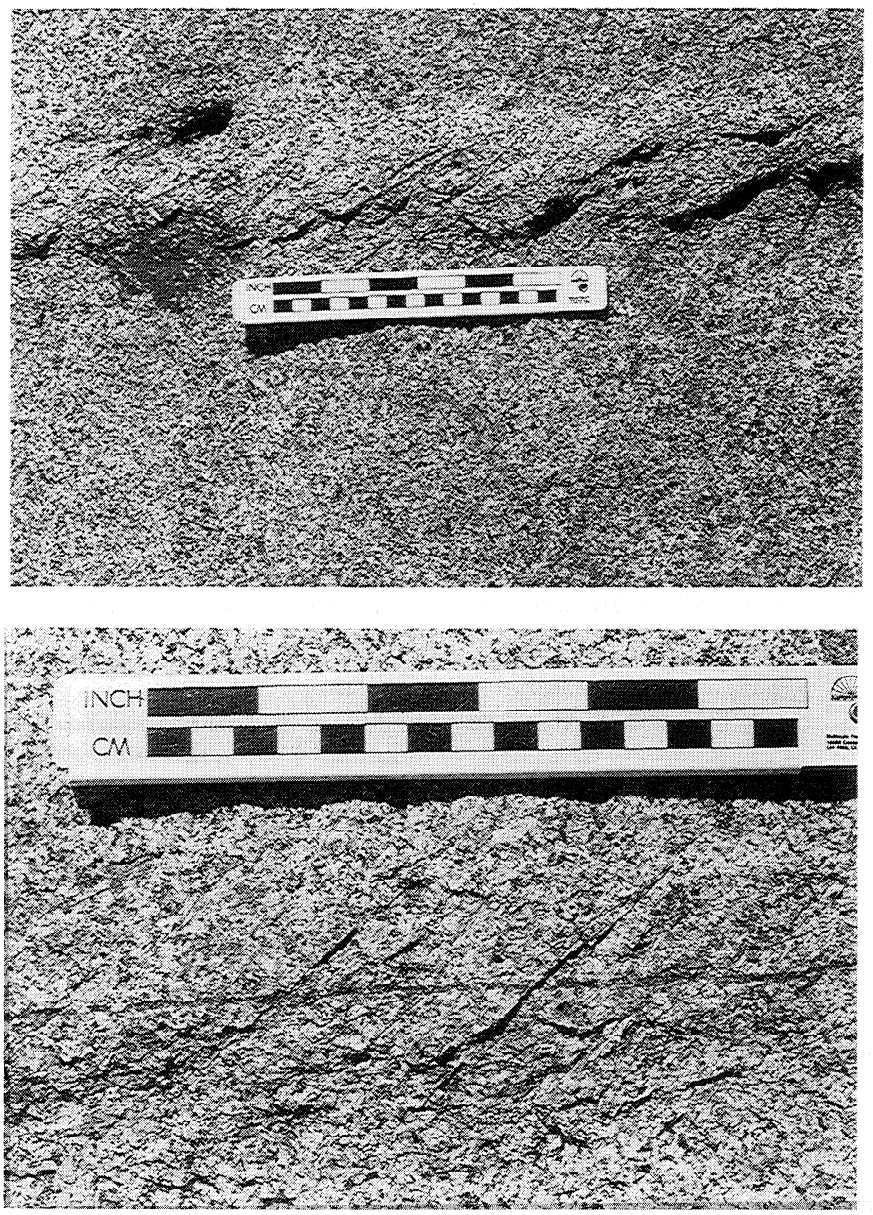

Figure 3. Photographs of a zipper crack band (a) without and (b) with a central fracture. The average strike of the band is N35°E. These structures are located at the Trail Junction Meadow outcrop of *Martel et al.* [1988].

4.1. LEFM and CZT Models

In LEFM, fractures are idealized as perfectly sharp features in a material capable of supporting infinitely large stresses [*Broek,* 1983], and inelastic deformation near the fracture edge is small [*Kanninen and Popelar,* 1985]. As a consequence of the exceedingly sharp tip of the fracture, a singular (infinite) stress concentration theoretically arises at the fracture edge [*Lawn and Wilshaw,* 1975; *Kassir and Sih,* 1975]. This so-called "near-tip" stress concentration dominates the stress field near the fracture edge. The near-tip stress concentration also has a characteristic form [*Lawn and Wilshaw,* 1975] that has been widely used to predict the orientation in which secondary fractures propagate [*Pollard et al.,* 1982; *Ingraffea,* 1987; *Cruikshank et al.,* 1991]. The precise character of the stress concentration depends on the mode of fracture, that is, the orientation of relative motion of the fracture walls with respect to the orientation of the fracture perimeter. For a vertical, penny-shaped strike-slip fault the relative motion at the 3:00 and 9:00 positions is perpendicular to the fault perimeter. This is pure mode II slip. The relative motion at the 12:00 and 6:00 positions parallels the fault perimeter. This is pure mode III slip. Locations at other places along the fault perimeter feel a mixture of mode II and mode III shearing. Mode I displacements correspond to opening of fracture walls; along an idealized smooth-walled fault the mode I displacements will be zero.

CZT was developed independently by *Dugdale* [1960] and *Barenblatt* [1962] to provide a mathematically tractable way to describe a physically plausible, finite stress concentration at the tip of an opening mode fracture in a linear elastic material. *Rudnicki* [1980] subsequently discussed application of CZT to faults. This theory postulates that elevated stresses, which resist the opening or sliding of fracture walls, occur in a "cohesive zone" just behind the fracture tip. If these resisting stresses are sufficiently strong and act over a sufficiently large portion of a fracture, they eliminate the theoretical singularity in stresses at the

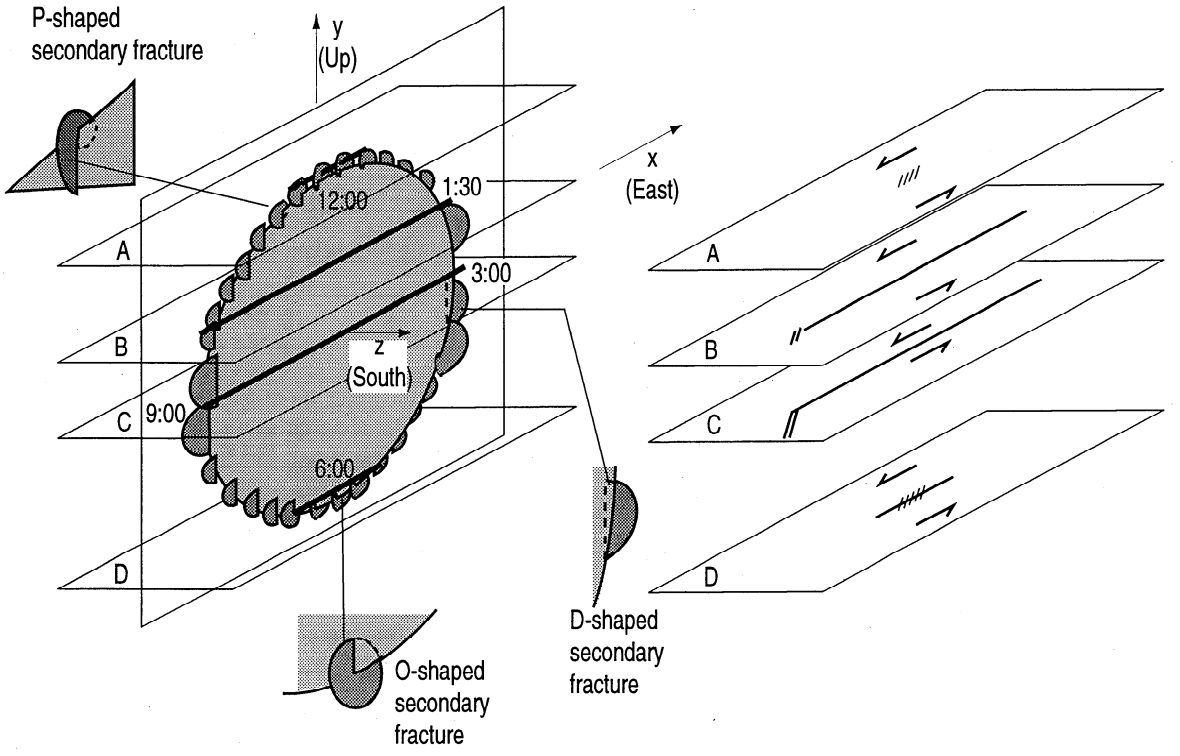

Figure 4. Conceptual model of a vertical penny-shaped strike-slip fault and secondary fractures.

fracture tip. The following equation describes this balance in two dimensions [*Martel,* 1997]:

$$\frac{\tau^{\infty}-\tau^{c}}{\tau^{\infty}-\tau^{f}}=\frac{-\sin^{-1}\left(\frac{a-R}{a}\right)}{\cos^{-1}\left(\frac{a-R}{a}\right)}. \qquad (1)$$

Here τ^{∞}, τ^{c}, and τ^{f} are the shear stresses parallel to the fault in the far-field, in the cohesive zones at the fault ends, and along the fault between the cohesive zones, respectively. The term a is the half length of the fault, and R is the length of the cohesive zone. The material outside the cohesive zone is considered to behave as a linear elastic material, but the material inside the cohesive zone need not be. The leading minus sign on the right side of (1) requires (τ^{∞} - τ^{f}) and (τ^{∞} - τ^{c}) to have opposing signs. This means that a shear stress drop at the fault center (τ^{∞} - τ^{f}) and a shear stress rise (τ^{∞} - τ^{c}) in the cohesive zone go hand-in-hand. For short cohesive zones (R<<a) the right side of (1) is large, meaning that the shear stress rise in the cohesive zone would be large relative to the shear stress drop at the fault center.

Two key implications of two-dimensional CZT in terms of secondary fracturing have been discussed recently [*Martel,* 1997]. First, along a fault with cohesive zones with a uniform shear stress, the peak principal tensile stress develops near the back of the cohesive zone away from the fault tip, rather than at the fault tip, and is finite. No secondary fractures would form if the tensile stress concentration were too small, but multiple secondary fractures could develop behind the tip of a fault trace if the tensile stresses were large enough [*Cooke,* 1997]. Second, if the stress drop during slip is low, then secondary fractures would tend to be nearly planar with a gently curved trace. This is because the orientations of the principal stresses near a cohesive zone are similar to those far from the fault. Two-dimensional CZT thus can account for a far wider range of secondary fracture locations and orientations than an LEFM model, and unlike LEFM, can account for the orientations of secondary fractures observed thus far in the field. A limitation of the two-dimensional theory is that it cannot fully describe the stress field around a fault that is bounded in size. This motivates a three-dimensional analysis.

In examining LEFM and CZT models in three dimensions, we consider a simple fracture geometry and use simple boundary conditions. We model a penny-shaped fault of radius a in an infinite, homogeneous, isotropic, linear elastic material. The cohesive zone, if present, is ring-shaped, with an outer radius $r=a$ and inner radius $r=b$ (Figure 5) For the sake of simplicity and to ease comparison with the Sierra Nevada faults, we consider a vertical, left-lateral strike-slip fault like that of Figure 4. The coordinate origin is at the fault center and the x and z axes are horizontal, the z axis being normal to the fault and the x axis being parallel to fault strike. The angle θ is measured in the plane of the fault about the z axis. At 12:00, θ =0. The angle α is measured in the horizontal plane about the y axis and equals zero along the positive x axis.

Boundary conditions are set using a tensor convention, with tensile stresses being positive. A uniform horizontal shear stress σ_{zx}^{∞} acts at a large distance from the fault and drives slip on the fault. Dimensionless far-field boundary conditions in our initial analyses are as follows:

$$\sigma_{zx}^{\infty}=\sigma_{xz}^{\infty}=-1, \qquad (2a)$$

$$\sigma_{xx}^{\infty}=\sigma_{xy}^{\infty}=\sigma_{yx}^{\infty}=\sigma_{yy}^{\infty}=\sigma_{yz}^{\infty}=\sigma_{zy}^{\infty}=0 \qquad (2b)$$

On the fault, two shear stress conditions are applied. In all cases,

$$\sigma_{zy}^{f}=0. \qquad (3)$$

The shear stress after slip along the portion of the fault ringed by the cohesive zone (i.e., $r<b$) is σ_{zx}^{f}, and the shear stress within the cohesive zone ($b<r<a$) is σ_{zx}^{c}. Based on work by *Sneddon* [1946] and *Kassir and Sih* [1975], the stress singularity at the perimeter

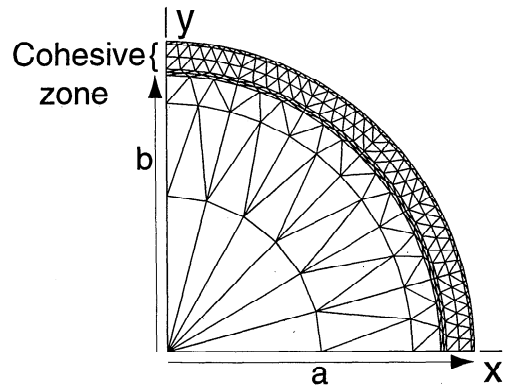

Figure 5. Geometry of elements used to define a vertical penny-shaped strike-slip fault with a cohesive zone. Only one quadrant of the total of 1320 elements is shown. The outermost four rings of elements define the cohesive zone. The z axis is normal to the fault and extends toward the viewer.

of a penny-shaped fault will be annulled if the following relationship holds [also see *Tada et al.,* 1973]:

$$\frac{\sigma_{zx}^{\infty} - \sigma_{zx}^{c}}{\sigma_{zx}^{\infty} - \sigma_{zx}^{f}} = \frac{-\left[a - \sqrt{a^2 - b^2}\right]}{\sqrt{a^2 - b^2}}. \quad (4)$$

The leading minus sign on the right side of (4) again requires (τ^{∞} - τ^{f}) and (τ^{∞} - τ^{c}) to have opposing signs. *Willemse* [1997] used an expression analogous to (4) and applied a Poisson's ratio of zero in his analyses. The choice of a Poisson's ratio of zero guarantees that the normal stress parallel to the fault perimeter ($\sigma_{\theta\theta}$) will not be singular, even if a cohesive zone is absent. However, the solutions of *Sneddon* [1946] indicate that if the stress singularity is annulled everywhere around the fault perimeter for σ_{zz} and σ_{rr}, the two other normal stresses orthogonal to $\sigma_{\theta\theta}$, then $\sigma_{\theta\theta}$ also will be nonsingular. Thus (4) holds for any value of Poisson's ratio. For a fault lacking a cohesive rim we initially assume that the shear stresses acting on the fault face are zero everywhere. For a fault with a cohesive rim the remote boundary conditions of (2) still apply, but shear stresses in the cohesive zone are set using (4).

In subsequent figures in this paper the cohesive zone inner radius b was set to $0.9a$. This cohesive zone size leads to secondary fracture distributions comparable to those observed along the small faults of Bear Creek (i.e., fracture clusters restricted to near fault trace ends).

4.2. Methods of Analysis

We use both analytical and numerical methods in our analyses. *Westman* [1965] provides closed form solutions for stresses in the plane of a penny-shaped shear fracture with a uniform resistance to slip in an infinite elastic medium. The solutions apply to a fault with no cohesive zone. We know of no simple analytical solution for the stresses around a penny-shaped fault with a cohesive zone. To treat a fault with cohesive zones, we applied the computer program Poly3D [*Thomas,* 1993], which is based on the boundary element method [*Crouch and Starfield,* 1983]. With Poly3D, the surface of a fracture is divided into a series of polygonal elements (Figure 5). The displacement discontinuity (e.g., slip) across a polygonal element is constant. To solve for the stresses around a fracture, one specifies either the tractions on each element, the relative displacements across the elements, or some combination of these conditions. In the first case, the relative displacements across the elements are calculated such that the stress boundary conditions are satisfied. Poly3D calculates stresses, strains, and displacements at observation points specified by the user as well as at the centroids of the polygonal elements.

Limitations of the original version of Poly3D necessitated some modifications of the code to solve the problems we posed. For example, *Crouch and Starfield* [1983] noted that boundary element methods yield accurate results only when observation points are either precisely on a boundary element or are farther than some minimum distance from an element. The minimum distance typically used is the length of an element. At this distance from a constant displacement-discontinuity boundary element the stresses typically are within a few percent of analytical solutions for problems with constant-stress boundary conditions. In the cases we tested, the elements were triangular. In order to obtain accurate solutions progressively closer to a fault, the triangle leg length can be shortened. However, rather than attempting to calculate stresses at observation points off the fault but very close to it (i.e., within an element leg length), we choose to calculate stresses at the element centroids. Although Poly3D does calculate directly the stress components acting on the elements at their centroids, it does not calculate the stress components acting parallel to the elements. Those stress components must be determined from numerical derivatives of the displacements of the centroids; these derivatives must be calculated with respect to two orthogonal directions [e.g., *Chou and Pagano,* 1967]. From these derivatives the strains can be calculated. A subsequent application of Hooke's law allows the desired stress components to be obtained from the strains. If the centroids were evenly spaced along a rectangular grid, then the desired numerical derivatives could be calculated straightforwardly. Unfortunately, only if the polygonal elements themselves are rectangular will their centroids be evenly spaced along a rectangular grid, and the smooth perimeter of a penny-shaped fault cannot be fit well with a small number of rectangular elements. We used a spline technique to approximate the element-parallel stress components (see the appendix for more details). Four rings of small elements were used for the cohesive zone to increase the resolution of the displacements there (Figure 5). This choice reduced but did not eliminate errors associated with a triangular element geometry, as described in the appendix.

We required that the fault walls remain in contact as they slip; they must be displaced equally in the z direction. The same result could be obtained by requiring both σ_{zz}^{∞} and the normal stress acting on the fault (σ_{zz}^{f}) to be zero, but only with a substantial penalty in terms of computer memory and run time.

4.3. Location of Secondary Fractures

We envision that secondary fractures nucleate around a fault where the tensile stresses are highest. The stress concentrations arising from slip die off with distance from the fault, so we focus on the vicinity of the fault plane. The magnitude of σ_1, σ_{xx}, and σ_{yy} are illustrated on the southern face of an east striking left-lateral fault with no cohesive rim in Figure 6. These stresses were calculated using the analytical solutions of *Westman* [1965]. The viewing direction is to the north. The plots also show the following. (1) On any horizontal traverse of the fault face, the tensile stresses are highest near the perimeter of the fault. (2) Inside the fault perimeter, the most tensile stress (σ_1) is highest near 9:00. (3) The stresses σ_{xx} and σ_{yy} are most tensile at 9:00 also; they are most compressive at 3:00. The first result suggests that if a secondary fracture nucleated on the wall of a fault, then it should nucleate toward the fault perimeter, where tensile stresses

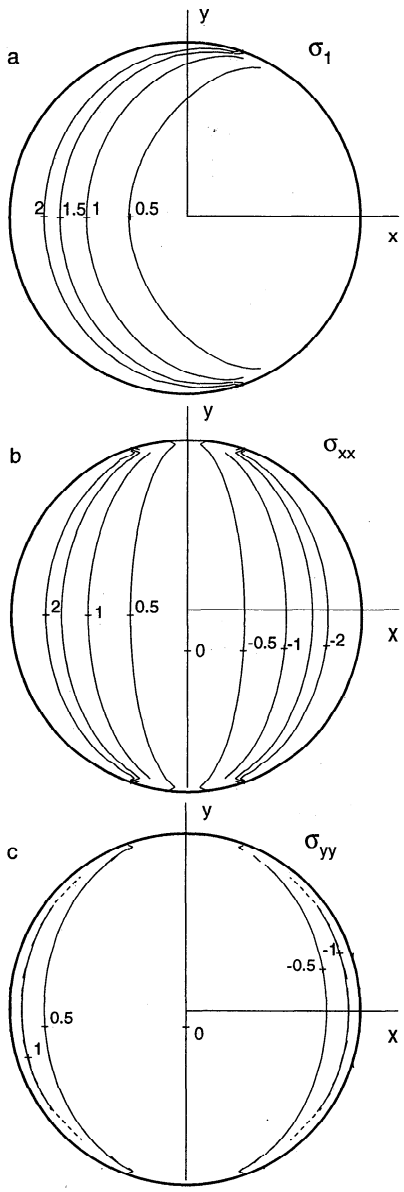

Figure 6. Dimensionless normal stresses on the face of a penny-shaped fault with no cohesive zone based on the analytical solutions of *Westman* [1965]. The faces of the fault sustain no shear stress. Stresses here and in subsequent figures are scaled relative to the far-field shear stresss σ_{zx}^{∞}. (a) The most tensile stress σ_1, (b) σ_{xx}, and (c) σ_{yy}.

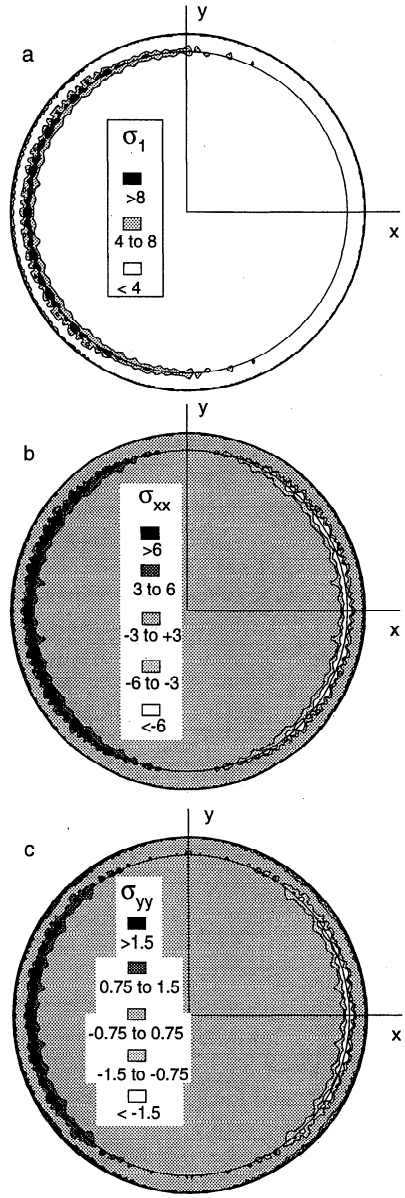

Figure 7. Dimensionless normalstresses on the face of a penny-shaped fault with a cohesive zone based on results from Poly3D. The portion of the fault ringed by the cohesive zone sustains no shear stress. (a) The most tensile stress σ_1, (b) σ_{xx}, and (c) σ_{yy}.

are greatest, rather than near the fault center. Furthermore, any secondary fracture that did nucleate on the fault face should preferentially propagate away from the fault equator toward the perimeter. Given that tensile stresses also are concentrated past the fault perimeter [*Kassir and Sih,* 1975], secondary fractures should be able to propagate some distance beyond the fault perimeter. These conclusions are consistent with the conceptual geometric model based on the field observations (Figure 4). The second result indicates that secondary fractures should preferentially nucleate, be more common, and be larger at 9:00 than at 12:00 and 6:00. This result is consistent with the scarcity of zipper crack bands and the relatively short length of the fractures in those bands. The third result indicates that if either preexisting horizontal fractures or fault-perpendicular vertical fractures occur near the fault perimeter, then they are most likely to be opened at 9:00 and closed at 3:00.

Although some predictions of LEFM are physically reasonable and are consistent with field observations, others are not. First and foremost, the singular nature of the LEFM crack tip stress field associated with a uniform driving stress is problematic on physical grounds. Second, owing to the theoretical singular stress concentration at the fault perimeter, all secondary fractures should nucleate at the fault perimeter rather than on the fault faces. Furthermore, because tensile stresses are highly concentrated past the perimeter of an LEFM fault, all secondary fractures nucleating at the fault perimeter should extend past the perimeter. Cases like Figure 2 appear rarely, however, suggesting that most fractures do not extend far past the fault perimeter. Third, secondary fractures should nucleate everywhere along the fault perimeter, making the lack of secondary fractures near the ends of many fault traces difficult to account for.

For a fault with a cohesive rim where the shear stress is uniform (Figure 7) the distributions of stresses are grossly similar to those for a fault lacking a cohesive zone, but there are two important differences. First, the stresses are finite, and thus the stress concentration is physically plausible and inherently broader than for the LEFM case. Second, the highest tensile stresses occur near the inner margin of the cohesive rim, rather than at the fault perimeter. This effect together with the prior one provide conditions favorable for the nucleation of secondary fractures over a larger portion of a fault than in the LEFM model.

4.4. Orientation of Secondary Fractures

We anticipate that secondary fractures grow such that they are oriented perpendicular to the most tensile local stress. Under LEFM constraints the singular stress concentration at the fault perimeter dominates the local stress field no matter how little a fault slips, and so the orientation of secondary fractures would depend only on the singular stress contribution arising from fault slip. However, LEFM does not yield predictions consistent with the observed orientations of secondary fractures. Based on the theoretical orientation of the most tensile stress near the perimeter of a penny-shaped LEFM fault, secondary fractures should strike away from a fault at an angle between 45° and 70°, the angle being measured relative to the strike of the fault. The angle should be near 45° [*Pollard et al.,* 1982] for pure mode III shearing (12:00 and 6:00 positions), and near 70° [*Ingraffea,* 1987] for pure mode II shearing (3:00 and 8:00 positions). Secondary fractures of these orientations are rare or absent along small faults of the Sierra Nevada. The observed intersection angles of the traces of secondary fractures and faults along Bear Creek are consistently 25°±10° (e.g., Figures 1, 2, and 3) rather than 45°-70°. If there is a component of opening along a fault (mode I relative displacement), then the predicted angle can be reduced. However, the amount of opening must be large relative to the amount of slip to lower the angle to the observed values near 25° [*Pollard et al.,* 1982; *Cruikshank et al.,* 1991], and the aperture:slip ratios of many Bear Creek faults are tiny [*Martel,* 1997]. Finally, LEFM predicts that as secondary fractures propagate, they should twist and warp to become perpendicular to the far-field most tensile stress [*Pollard et al.,* 1982]. In contrast, the field observations suggest that the secondary fractures twist little if at all. The field observations and the predictions of LEFM thus conflict in several key qualitative and quantitative areas.

For a fault with a cohesive zone the orientation of a secondary fracture would be determined by the total stress field, not just the perturbation to the stress field arising from fault slip. The total stress field reflects contributions from gravity, regional tectonic stresses, thermal stresses, and the perturbations arising from slip on the fault.

To simulate these effects, we consider the following dimensionless far-field boundary conditions, scaled relative to the magnitude of the far-field shear stress σ_{zx}^{∞}:

$$\sigma_{zx}^{\infty} = \sigma_{xz}^{\infty} = -1, \quad (5a)$$

$$\sigma_{xy}^{\infty} = \sigma_{yx}^{\infty} = \sigma_{yz}^{\infty} = \sigma_{zy}^{\infty} = 0, \quad (5b)$$

$$\sigma_{xx}^{\infty} = -2 \tan(2\alpha), \quad (5c)$$

$$\sigma_{yy}^{\infty} = -\tan(2\alpha) - 1, \quad (5d)$$

$$\sigma_{zz}^{\infty} = 0. \quad (5e)$$

These conditions lead to strike slip along a vertical fault (Figure 8). The most tensile far-field principal stress (σ_1) and most compressive principal stress (σ_3) are horizontal; α gives the orientation of the most compressive stress as measured counterclockwise from the strike of the fault. In our case, α = 25°. The intermediate principal stress (σ_2) equals σ_{yy} and is vertical and compressive (negative). The magnitude of σ_{yy} is arbitrarily set such that the difference between it and the mean normal stress equals the magnitude of the shear stress σ_{zx}^{∞}. These choices yield a unit left-lateral shear stress and no normal stress along planes parallel to but remote from the fault (Figure 8).

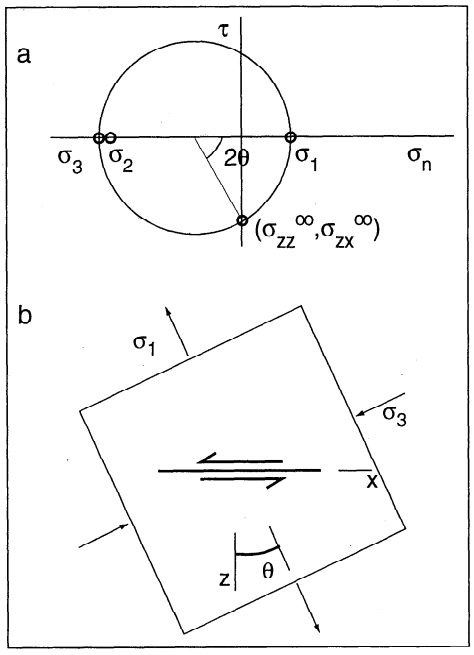

Figure 8. Far-field stress state used in calculations. (a) Mohr circle diagram. Tensile normal stresses and right-lateral shear stresses are considered positive. The angle α between the σ_1 direction and the normal to the fault is 25°. The most tensile stress (σ_1) and the least tensile stress (σ_3) are horizontal, and the intermediate principal stress (σ_2) is vertical. The difference between the intermediate principal stress and the mean normal stress equals the magnitude of the far-field shear stress parallel to the fault (σ_{zx}^{∞}). (b) View down on the fault (in the negative y direction) showing the orientation of σ_1 and σ_3 relative to the fault and the reference frame.

Figure 9 depicts predicted secondary fractures around a penny-shaped strike-slip fault. The secondary fractures are represented by semicircular disks as seen in orthographic projections parallel to the fault. The fractures appear most foreshortened where their strike is most nearly perpendicular to the fault. A dot marks the center (and inferred nucleation point) of each secondary fracture. These centers are located along the inner radius of the cohesive zone, where the most tensile stress is at a maximum along a radial line from the fault center. Far-field boundary conditions are given in (6) and Figure 8. Figures 9a and 9b thus show predicted fracture orientations if no vertical stress were applied (i.e., if gravitational stresses were ignored). In Figures 9c and 9d the vertical stress is given by (6d). In Figures 9a and 9c the shear stress drop at the fault center is 100% (i.e., $\sigma_{zx}^{f} = 0$ for $r<b$), whereas in Figures 9b and 9d the stress drop is 1% (i.e., $\sigma_{zx}^{f} = 0.99\sigma_{zx}^{\infty}$). *Martel* [1997] noted that the stress drop during slip on a fault should affect the strike of secondary fractures; Figures 9a-9d show that the dip is affected too. They also show that a low stress-drop CZT model is consistent with observed macroscopic fracture orientations at Bear Creek, whereas high stress drops are inconsistent. A low stress drop also is consistent with the ductile

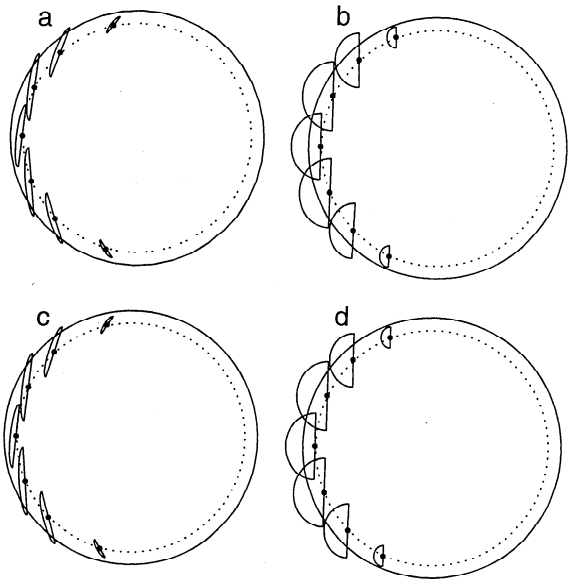

Figure 9. Predicted orientations of potential secondary fractures along a penny-shaped fault; far-field most compressive stress at 25° to fault. Secondary fractures are depicted as foreshortened semicircles and are oriented perpendicular to the local most tensile stress σ_1. Dots mark the centers of the secondary fractures. Fracture radii are scaled to the magnitude of the most tensile stress. The view here is perpendicular to the fault, so the secondary fractures, which do not parallel the fault, appear foreshortened. The inner radius of the cohesive zone (dotted line) is set to 90% of the fault radius. (a) Unit stress drop; $\sigma_{yy}^{\infty} = 0$. (b) Stress drop of 1%; $\sigma_{yy}^{\infty} = 0$. (c) Unit stress drop; σ_{yy}^{∞} as shown in Figure 8. (d) Stress drop of 1%; σ_{yy}^{∞} as shown in Figure 8a. The secondary fractures in Figures 9b and 9d strike 25°±3° relative to the faults and dip at nearly 90°.

mylonitic fabrics of the material filling the small faults [*Segall and Pollard,* 1983].

4.5. Distribution and Shapes of Secondary Fractures

The distributions and shapes of secondary fractures can be gauged by the strength and distribution of the tensile stress concentrations depicted in horizontal and vertical cross sections perpendicular to a fault. Figure 10 shows the magnitude of the most tensile stress and trajectories (large tick marks) normal to the most tensile stress along the four horizontal planes perpendicular to the fault of Figure 4. The trajectories reflect the most probable strike of new secondary fractures that open. Figure 11 shows the stress configurations along the four vertical planes that intersect the fault near 3:00 and at 1:30, 12:00, and 8:30; the locations of the planes are shown as insets. Fault traces on Figure 11 are shown in a heavy line, and small ticks crossing a fault trace mark limits of the cohesive zones. Dotted lines show the diameter of the faults. The boundary conditions of Figures 10 and 11 are those of Figure 9d which correspond to a 1% shear stress drop and a most tensile far-field stress of dimensionless magnitude 0.4663.

Local tensile stresses with magnitudes greater than the most tensile far-field stress would promote secondary fracture formation, whereas lower stresses would not. Regions where σ_1^{local} exceeds the most tensile far-field stress of 0.471 are shown shaded in Figures 10 and 11. These regions correspond roughly to where secondary fractures were observed in the field, but they are larger, relative to the fault, than the regions of observed fracturing. Smaller regions that more closely fit the sizes of the observed regions of fracturing would be bounded by higher stress levels and have similar shapes to those shown but would be difficult to see in Figures 10 and 11.

Figure 10 suggests how secondary fractures would be distributed along the strike of a fault trace. For planes at 3:00 (Figure 10c) and 1:30 (Figure 10b) the most tensile stress is concentrated near the fault trace ends and diminishes rapidly toward the fault trace center. Secondary fractures intersected by either of these planes would likely be concentrated near the fault trace ends. If multiple secondary fractures were encountered, then their traces would decrease in length toward the fault trace center. In contrast, the magnitude of the most tensile stress is much more uniform along strike near the top and bottom of the fault (Figures 10a and 10d, respectively). Secondary fractures near the top or bottom of a strike-slip fault thus seem more likely to have a spatial distribution and horizontal trace length distribution more uniform than for fault end secondary fractures. These predictions are in general agreement with the observations.

Figures 10 and 11 together provide some insight into likely shapes of secondary fractures. The D-shaped secondary fractures of Figure 4 occur near 3:00 and 9:00. They are confined to one side of the fault. In this sense they are like edge cracks that extend from free surfaces and characteristically assume semielliptical shapes [*Broek,* 1993]. The portions of the shaded regions of Figures 11a and 11d that are restricted to the sides of the fault with the broader tensile stress concentrations are also D-shaped. A comparison of the shaded areas in Figures 10a and 10d and those of Figures 11c and 10b indicates that the D-shaped fractures are likely to have a significantly greater vertical extent than horizontal extent. The O-shaped fractures of Figure 4 occur near 6:00 and 12:00. They extend past the perimeter of the fault, across the fault plane, and toward the fault equator. The roughly equidimensional shaded areas in Figure 11c reflect stress concentrations at 6:00 and 12:00 that would promote formation of a roughly O-shaped fractures centered near the fault perimeter. The P-shaped fractures of Figure 4 occur near 1:30, 4:30, 7:30, and 10:30. These are inferred to be asymmetric, with large lobes on the sides of the fault with the broader tensile stress concentrations and small lobes extending to the other side of the fault. Elasticity theory predicts that perturbations of the normal stress components arising from fault slip are of opposite sign on the opposing walls of a fault [*Pollard and Segall,* 1987], so one might suspect that secondary fractures would be strongly hindered in propagating from the side of a fault where the mean tensile stress is increased as a result of slip to the opposing side where the mean compressive stress is increased [see *Pollard and Segall,* 1987, Figure 8.7b]. However, the stress field near the end of a fracture is complex, and concentrations of the most tensile stress in fact do develop where the mean compressive increases, albeit of smaller extent than those on the side where the mean tensile stress increases. Figures 10b, 10c, 11b, and 11c of this study show this, as do Figures 7b and 11 of *Segall and Pollard* [1980]. Thus secondary fractures nucleating on one side of a fault should be able to propagate past the perimeter of the fault and a small distance across the fault plane to yield P-shaped secondary fractures. Figure 11b suggests that the horizontal and vertical extents of these P-shaped fractures would be similar.

4.6. Relative Sizes of Secondary Fractures

The observed relative sizes of secondary fractures also can be gauged by the extent of tensile stress concentrations around the fault. The field observations show that the traces of secondary

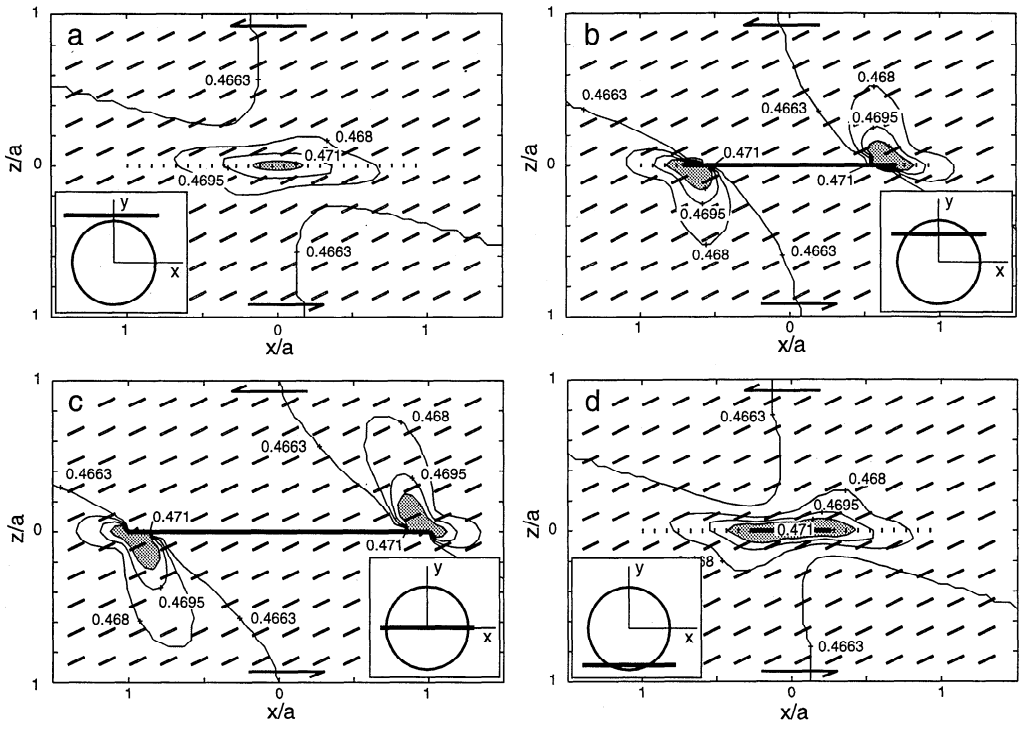

Figure 10. Contour map of the magnitude of the most tensile stress (σ_1) and trajectories normal to σ_1, along horizontal planes perpendicular to a model penny-shaped fault of radius a. Boundary conditions match those of Figure 9d. Insets show where cross-section planes cut fault. (a) Plane is a distance of $0.03a$ above the top of the fault. Compare with plane A of Figure 4. (b) Plane intersects fault at 1:30. Compare with plane B of Figure 4. (c) Plane intersects fault at 3:00 and 9:00. Compare with plane C of Figure 4. (d) Plane is a distance of $0.03a$ above the bottom of the fault. Compare with plane D of Figure 4.

fractures are roughly an order of magnitude longer near fault trace ends than along the zipper crack bands. We interpret these observations as indicating that D-shaped fractures near 3:00 and 9:00 will have much greater horizontal extents than O-shaped fractures near 6:00 and 12:00. Suppose secondary fractures extend from a fault and terminate where the most tensile stress drops below the most tensile far-field stress, which is 0.471 in Figures 10 and 11. Figures 10 and 11 suggest that the D-shaped fractures would have horizontal extents greater than O-shaped fractures, but not an order of magnitude greater. The 0.471 contour also encloses a region that extends considerably farther from the trace of the model fault than the observed secondary fractures extend from the real fault traces. This suggests a higher stress threshold for secondary fracturing is appropriate. A higher threshold also would account for the inherent tensile strength of the rock. In Figures 12a and 12b we consider a contour of 0.4715, which hugs the fault tighter than the 0.471 contour and encloses an area more compatible with the regions of secondary fractures observed in the field. In Figure 12a, which represents conditions near the top of the fault, this contour extends a distance of about 0.01a away from the projected fault trace, about half the distance of the 0.471 contour. In contrast, in Figure 12b, which represents conditions near 9:00, this contour extends a distance of about $0.15a$ away from the fault trace, the distance being measured along the strike of potential secondary fractures. Thus if secondary fractures propagated to the 0.4715 contour, their maximum horizontal dimension near 3:00 and 9:00 would be several times the horizontal dimension near 6:00 and 12:00. This is comparable to the relative lengths of the observed fractures. If a higher contour level were selected, the disparity would increase. The D-shaped fractures (Figures 11a and 11d) are expected to have greater heights than the O-shaped fractures (Figure 11c), and this would also contribute to a greater horizontal extent of the D-shaped fractures. If the fault were elliptical and longer than it is tall, rather than circular, that would also promote the formation of larger D-shaped fractures owing to relatively enhanced stress concentrations near 3:00 and 9:00 [*Kassir and Sih,* 1975].

4.7. Evaluation of LEFM and CZT Models

In conclusion, although LEFM and CZT models are qualitatively similar in several ways, CZT has some distinct advantages. First, it is more plausible on physical grounds because the predicted stress concentrations are finite. Second, it more readily accounts for the observed locations, orientations, and sizes of secondary fractures. Third, it better explains the presence of multiple fractures near the end of a fault trace owing to its broader, finite concentration of tensile stress near the fault perimeter.

A three-dimensional CZT model has some key advantages over a two-dimensional model. First, a three-dimensional model can treat faults and fractures of finite size. As a result, it provides an even more robust explanation for the multiple secondary fractures observed near the ends of many fault traces. Secondary fractures in a two-dimensional model would have an infinite height; opening such a fracture would reduce the local tensile stresses and inhibit the opening of other fractures nearby, more so than the opening of a three-dimensional fracture of finite height. Multiple fractures thus are more likely to form in a given volume of material along the fault perimeter if they are of finite size.

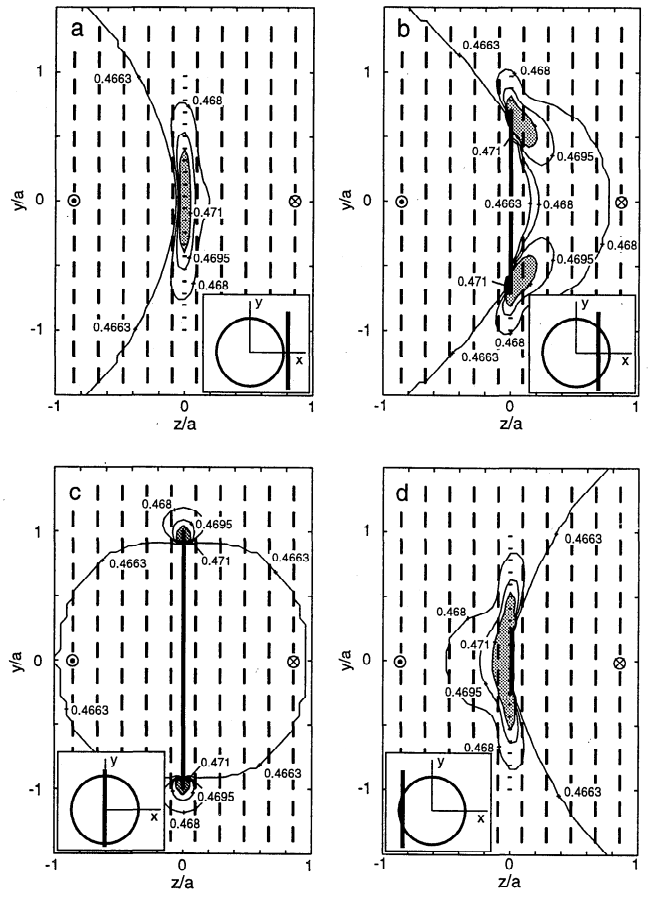

Figure 11. Contour plot of the magnitude of the most tensile stress (σ_1) and trajectories normal to σ_1, along vertical planes perpendicular to a model penny-shaped fault of radius a. View is along strike to the west. Boundary conditions match those of Figure 9d. Insets show where cross-section planes cut fault. (a) Plane is a distance of $0.03a$ past the 3:00 end of the fault. (b) Plane intersects fault at 1:30. (c) Plane through 6:00 and 12:00. (d) Plane a distance of $0.03a$ toward the fault center from 9:00.

Second, the three-dimensional model provides a unifying explanation for the locations, orientations, and sizes of a broader range of secondary fractures (see Figure 4). The two-dimensional model of *Martel* [1997] accounts only for secondary fractures that form in response to pure mode II loads, whereas a three-dimensional model accounts for mode II, mode III, and mixed-mode II-III loads. A three-dimensional CZT model thus can account much better for the locations, orientations, sizes, and relative abundances of secondary fractures observed in the field.

5. Discussion

Questions regarding how secondary fractures along faults can be located and characterized, how they affect fluid flow, and how they can be predicted stimulated our work. Our discussion of the field observations and mechanical analyses focuses on five specific points relevant to those questions.

5.1. Hydrogeologic Effects of Secondary Fractures Along Bear Creek

Theory shows that secondary fractures have the potential to radically change the hydrogeologic behavior of a rock mass [e.g., *Long and Witherspoon,* 1985]. Field observations indicate that such "replumbing" did occur over a rather broad scale in the main pluton along Bear Creek, the Lake Edison Granodiorite. The main evidence is in the distribution of quartz along fractures in the pluton. As noted in section 2, quartz fillings are rare along the mineralized, unfaulted joints but are common along the faults and associated secondary fractures. This indicates that faulting in some way profoundly affected the hydrogeologic behavior of the pluton. Two competing scenarios for how this might have occurred seem most likely. First, where fault slip produced localized regions of elevated mean compressive stress (e.g., on the side of a fault immediately opposite a secondary fracture), quartz might have liberated from the host granodiorite by pressure solution. Quartz dissolved from these regions conceivably could have been transported by fluids to, then precipitated in, the adjacent fault and the secondary fractures. Second, in contrast to unlinked joints, faults linked by secondary fractures might have become large, hydraulically well-connected systems able to sample and conduct quartz-rich fluids from a remote source, such as an adjacent intruding pluton. *Bürgmann and Pollard* [1994] tested and rejected the first possibility on the basis of geochemical analyses; there was no evidence of preferential quartz loss opposite secondary fractures near fault trace ends. Unless another viable explanation can be found, the linkage of originally discontinuous, parallel faults by secondary fractures to form a well-connected, conductive fracture network appears to be the most likely mechanical explanation for why quartz is scarce in the joints and common in the faults. Further geochemical work in the Bear Creek region might be able to substantiate this.

5.2. Loading Conditions During Faulting

Some general comments on the loading conditions during slip along the faults of Bear Creek can be made based on the orientations of the secondary fractures. The secondary fractures there consistently strike 25°±10° counterclockwise relative to their host faults, even though the absolute orientations of the faults vary. For example, faults at the Kip Camp outcrop of *Segall and Pollard* [1983] strike about N65°E, whereas the central fracture of Figure 2b of this study strikes N35°E. We assume that the secondary fractures strike roughly perpendicular to the most tensile far-field stress and parallel to the most compressive

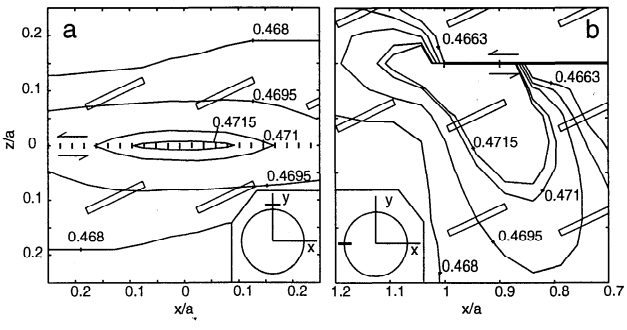

Figure 12. Contour map of the magnitude of the most tensile stress (σ_1) and trajectories normal to σ_1 along horizontal planes perpendicular to a model penny-shaped fault of radius a. Boundary conditions match those of Figure 9d. Insets show where cross-section planes cut fault. Contour levels match those of Figure 10, except for the addition of a contour at 0.4715. (a) Plane is a distance of $0.03a$ above the top of the fault. Compare with Figure 10d. (b) Plane intersects fault at 9:00. Compare with Figure 10c.

horizontal stress at the time of faulting. The varied absolute orientations of the secondary fractures thus indicate that different faults slipped when the far-field stresses were at different orientations. This means that different faults slipped at somewhat different times, so the far-field principal stresses probably were rotating about a vertical axis during the general period of faulting; this is consistent with findings by *Christiansen* [1995]. Additionally, the narrow orientation range of the secondary fractures relative to their host faults implies that the faults tended to slip when the most compressive horizontal stress was oriented at 25°±10° relative to fault strike. This is about what one would predict using standard Mohr-Coulomb shear failure criteria for rocks lacking preexisting planes of weakness. Perhaps conditions during faulting were such that the faults were only slightly weaker than the host rock. This condition might not be peculiar to the faults of Bear Creek, for secondary fractures along small faults in other areas also formed at angles of 25°±10° relative to the host fault [e.g., *Granier,* 1985; *Martel and Peterson,* 1991].

5.3. Comparison With Models Based on Laboratory Investigations

Conceptual models of secondary fractures around penny-shaped shear fractures have been prepared by other investigators based on laboratory experiments and are illustrated in Figure 13. *Adams and Sines* [1978] based their conceptual model (Figure 13a) on compression tests on penny-shaped cracks in rectangular plastic samples. The cracks were machined into the surface of two blocks of polymethylmethacrylate plastic (PMMA) that were subsequently glued together, so the cracks were along a seam. The samples were loaded in uniaxial compression tests, with the axis of compression at 45° to the penny-shaped cracks. In some of their tests the samples were clamped in a vise to produce a biaxial compression, with the resulting intermediate compressive stress being parallel to the crack. The magnitude of the compressive stress produced by the vise apparently was not measured. *Scholz* [1990] crafted his conceptual model (Figure 13b) by combining results of two-dimensional mode II shear tests in plastic sheets [e.g., *Brace and Bombolakis,* 1963] with mode III torsion tests on rocks [*Cox and Scholz,* 1988a, b]. *Germanovich et al.* [1994] based their conceptual model (Figure 13c) on uniaxial compression tests on PMMA and silica glass. Their penny-shaped cracks were formed inside the samples using a laser and thus did not lie along a seam. The laser produced a powder along the crack faces in the PMMA samples but not in the glass. Cracks grew more stably in the PMMA samples than in the glass, which tended to fail explosively. Germanovich and his colleagues concluded that high friction between the crack faces in the glass impeded sliding, whereas the soot probably acted as a lubricant between the crack faces in the PMMA and promoted sliding.

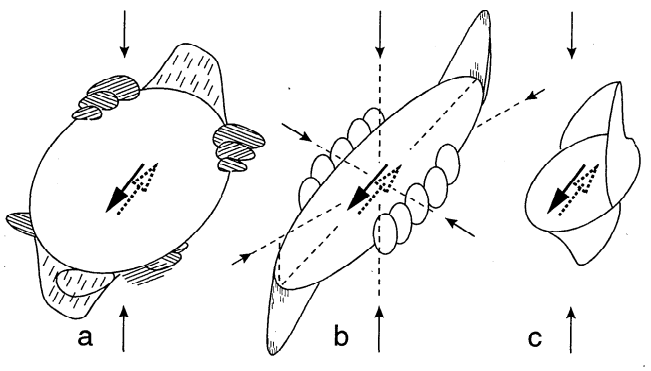

Figure 13. Secondary fracturing models from (a) *Adams and Sines* [1978], (b) *Scholz* [1990], and (c) *Germanovitch et al.* [1994]. Modified from *Germanovitch et al.* [1994]. Small solid arrows show orientations of applied compressive stresses. Figure 13a is reprinted from *Adams and Sines* [1978]. Copyright 1978 with permission from Elsevier Science.

The secondary fractures in Figures 4 and 13 have three key similarities regarding locations, orientations, and sizes. (1) They touch the penny-shaped shear fracture near its perimeter. (2) They are roughly perpendicular to the most tensile principal stress on the sample boundary. (3) They are larger where the fracture perimeter is perpendicular to the slip vector (i.e., 3:00 and 8:00) than where it parallels the slip vector (i.e., 6:00 and 12:00). These similarities are consistent with the descriptions in section 5 regarding the stress concentrations along the perimeter of a penny-shaped shear fracture and with the numerical results of *Germanovich et al.* [1996].

There are also some key differences between the conceptual models, however. First, the secondary fractures at 9:00 (mode II loads) in Figure 4 are planar, do not everywhere intersect the fault at its perimeter, and do not merge to form a continuous curved fracture, in contrast to those in Figure 13. The model of Figure 4 accounts for multiple discontinuous secondary fractures near the end of a fault trace, whereas the models of Figure 13 cannot. Second, the P-shaped secondary fractures of Figure 4 provide an explanation for secondary fracture traces that occur past the end of a fault trace; none of the corresponding fractures in Figure 13 can. Third, Figure 4 can account for the presence of zipper crack bands with and without central fractures. Neither Figure 13a nor 13c can account for a zipper crack band at all, and Figure 13b cannot account for a band with a central fracture. Interestingly, *Cooke and Pollard* [1996] did produce secondary fractures in their experiments that resembled those near 12:00 of Figure 4, with secondary fractures propagating ahead of as well as behind the shear fracture front, but the portions behind the shear fracture front were difficult to photograph (M. L. Cooke, personal communication, 1997). The experiments of *Cooke and Pollard* [1996] thus support a pattern like that near 12:00 and 6:00 of Figure 4. So although the models of Figures 4 and 13 are similar in several ways, only Figure 4 captures the details necessary to match the field observations in Bear Creek.

The differences between the conceptual models of Figures 4 and 13 might be largely a result in differences in the loading conditions during slip in the Earth and in the laboratory. Neither *Adams and Sines* [1978] nor *Germanovich et al.* [1994] applied large triaxial compressive loads in their laboratory tests. Instead, compressive stresses were applied to either one or two faces of the plastic parallelepipeds containing the fractures. Where compression was applied to two sample faces [*Adams and Sines,* 1978], one of the directions was parallel to the shear fracture. An inspection of Figure 9 shows that applying an intermediate compressive stress parallel to a shear fracture will have relatively little effect on the orientation of secondary fractures. The loads that *Adams and Sines* [1978] and *Germanovich et al.* [1994] applied might not have been sufficient to close the shear fractures tightly. If a shear fracture were not closed, it would sustain no shear stress. Thus the experimental conditions might correspond to the large stress-drop scenarios of Figures 9a and 9b. Figures 9a and 9b show a large stress drop is far more likely to yield continuous curved secondary fractures near 3:00 and 9:00 than a small stress drop is (Figures 9c and 9d). Thus the discrepancies

between the models of Figures 4 and Figure 11 might be due primarily to differences in loading that yielded differences in the stress drops during slip.

The method of sample construction probably accounts for some discrepancies too. For example, *Adams and Sines* [1978] show all the secondary fractures that extend past the perimeter of the penny-shaped shear fracture as being D-shaped (Figure 13a). The seam along the penny-shaped crack in their test might well have prevented those secondary fractures from propagating across the plane of the fault and becoming P-shaped as our analyses predict. The powder on the faces of the penny-shaped fractures of *Germanovich et al.* [1994] might have acted as a dry lubricant, favoring a large stress drop during slip.

Although differences in loading rates, material rheology, and environmental conditions probably contribute to some differences between field-based observations and laboratory-based models, triaxial compression tests with loads sufficient to close a shear fracture could help resolve whether the differences are primarily a reflection of different loading conditions. Alternatively, a weak bonding resin might be injected into a laboratory shear fracture to allow for slip with an incomplete stress drop.

5.4. Comparison of Two- and Three-Dimensional Mechanical Models

The three-dimensional nature of our mechanical analysis required us to address some issues that two-dimensional analyses did not. For example, the two-dimensional plane-strain analyses of *Segall and Pollard* [1980] and *Pollard and Segall* [1987], if applied to strike-slip faults, pertain to vertical faults. Owing to the two-dimensional nature of those analyses, the secondary fractures that the analyses predict must be vertical too. The question of what might have caused the secondary fractures along the faults of Bear Creek to actually be nearly vertical tends not to arise in a two-dimensional analysis. Our three-dimensional analyses prompted us to account for the effects of three principal stresses in order to explain the observed dip of the secondary fractures. An inspection of Figure 9 shows that the stress drop during slip will greatly affect the orientation of the secondary fractures, whereas the vertical stress due to the weight of the overburden exerts little influence if it is the intermediate principal stress.

5.5. Implications Regarding Fault Growth and Fault Hydrology

The mechanical model proposed here has direct implications for how faults link, grow, and conduct fluids in three dimensions. Both field observations and mechanical considerations indicate that strike-slip faults far from a free surface in massive granitic rock should link more readily end-to-end than top-to-bottom (Figure 14). This is because fractures associated with mode II loads are larger than those for mode III.

Although our focus here is on the linkage of neighboring segments of small strike-slip faults, linkage is increasingly recognized as being a significant, or potentially significant, process in the growth of faults of all types across a broad range of scale [*Childs et al.*, 1996; *Cladouhos and Marret*, 1996; *Mansfield and Cartwright*, 1966; *Nicol et al.*, 1996; *Wojtal*, 1996]. We expect a strike-slip fault formed by linkage in massive granitic rock would tend to develop its maximum dimension along strike if growth were unrestricted, whereas a dip-slip fault would tend to develop its greatest dimension downdip. Unfortunately, information on aspect ratios for faults with dimensions of kilometers is exceedingly scarce for massive granitic rock. This precludes a thorough discussion of scaling in this type of rock.

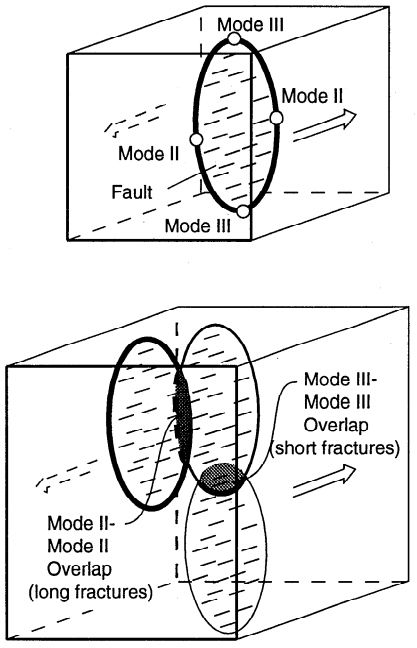

Figure 14. Possible locations of fault linkages, shown here for idealized penny-shaped strike-slip faults. Mode II-mode II linkages are oriented perpendicular to the slip vector. Mode III-mode III linkages are oriented parallel to the slip vector.

The available data on faults with dimensions of kilometers instead tend to come from heterogeneous or layered rocks. The data presented by *Nicol et al.* [1996] show that both normal and strike-slip faults (or fault ruptures during earthquakes) tend to have greater dimensions in the direction of strike than the direction of dip. In their study of normal faults in sedimentary rocks, *Mansfield and Cartwright* [1996] concluded that initially isolated dip-slip faults had dimensions parallel to layering (along strike) several times greater than across layering (downdip). This is counter to our prediction for faults in massive rock and instead is reminiscent of the relative dimensions of strata-bound joints in sedimentary rocks [e.g., *Pollard and Aydin*, 1988]. We contend that the discrepancy is not a function of scale but rather a reflection of the mechanical difference between massive granitic rock and layered rock, consistent with the conclusions of *Nicol et al.* [1996].

Forster and Evans [1991] have previously argued that the hydraulic conductivity of faults should be anisotropic, with the hydraulic conductivity across a fault in many cases being much lower than the conductivity parallel to the fault. Our work suggests that fluid flow along faults would tend to be anisotropic and channeled, with "chimneys" of highly fractured rock oriented normal to the slip vector being regions of elevated hydraulic conductivity (Figure 14). This point also has been noted previously by *Martel and Peterson* [1991] and *Sibson* [1996]. For vertical strike-slip faults these chimneys would be vertical. We expect horizontal linkages between the top and bottom of overlapped strike slip faults (i.e., parallel to the slip vector) also will exist. However, based on the narrowness of the zipper fracture bands (Figure 3) and our modeling studies, these slip-parallel linkages would be less well developed or smaller than linkages normal to slip, especially where slip along the linked faults is small. Hence fault plane hydraulic conductivity arising from linkages would be high parallel to slip and low normal to slip. This prediction contrasts with what one might expect based

on studies of fault roughness. For example, *Power et al.* [1987] and *Lee and Bruhn* [1996] have called attention to how faults tend to be substantially smoother in the direction of slip (i.e., in the orientation of slickenlines) than in the direction normal to slip. Calculations of *Brown* [1987] and *Thompson and Brown* [1991] have shown that fluids would flow more readily along the less tortuous path; along strike-slip faults this would be horizontally rather than vertically. There is no obvious reason why anisotropy both in linkages and in fault roughness should not contribute to anisotropy and channeled fluid flow along faults, but their relative importance probably is a function of location, scale, and perhaps the amount of slip.

Our model also is being adapted to stochastic use. For example, distributions of secondary fracture locations and sizes can be selected stochastically using the most tensile stress or the strain energy density. Estimation of statistical parameters describing the distributions of fault and fracture sizes can be done by conditioning the statistical model to match field data using a method called conditional coding [*Hestir et al.*, 1998]. The estimation results can be used to determine connectivity of the fault zone and as a basis for hydrologic inverse modeling [e.g., *Martel and Evans*, 1996; *Hestir et al.*, 1998].

6. Conclusions

Observations of the structure and mineral fillings along the small faults and secondary fractures along Bear Creek indicate that secondary fractures played a critical role in fault growth and fluid flow. The three-dimensional model we propose for secondary fractures is consistent with field observations from Beer Creek. It also is consistent with a physically plausible, quantitative CZT model for fracturing in three dimensions around faults. Finally, the model is compatible in many ways with results from laboratory experiments on shear fractures in plastics. Differences between the laboratory results and the field observations underscore some of the considerations which must be accounted for if laboratory tests on shear fractures are to be used to precisely simulate faulting at depth in the Earth. Our observations, conceptual geometric model, and three-dimensional CZT model together provide a way to account for and predict the location, relative extent, orientation, and relative abundance of secondary fractures along the small faults of Bear Creek. The style of secondary fracturing there is reflected along faults in crystalline rocks in other parts of the world. Accordingly, our model should have broad applicability in understanding how fluids flow along faults and how faults grow in crystalline rock.

Appendix

To calculate strains on the faces of a fracture defined by polygonal displacement discontinuity elements, one must obtain the partial derivatives of the element-face displacement field along two orthogonal directions. For each element we sample the displacement field at the element centroid and at two points just outside the element perimeter, one along the axis of strike and the other along the orthogonal axis of dip. The displacements and coordinates at these points are used with B splines [e.g., *Kincaid and Cheney*, 1991] to calculate the partial derivatives at the centroid. The orders of B splines are designated by a superscript. The lowest orders, B^0 and B^1, are used here. B^0 splines are piecewise constant functions, whereas B^1 splines are piecewise linear. Everywhere B^1 splines exist they have derivatives, except at the ends of their constituent line segments.

Figure A1 provides an example of spline usage. The upper part of Figure A1 shows a cartoon of some triangular Poly3D elements and a reference line, L. The lower part shows a graph of one displacement component (u) as a function of position (x) along L. Displacements are constant on the face of an element, so that graph consists of piecewise constant segments. Connecting the right edges of these segments by dotted lines produces a piecewise linear graph. These two graphs can be represented by B^0 and B^1 spline functions, respectively. Segment endpoint coordinates x_i are assumed to be in ascending order but need not be evenly spaced. The corresponding displacements are u_i. Consider a point x such that $x_i < x < x_{i+1}$. The derivative of the B^1 spline evaluated at x is given by equation (A1), as adapted from *Kincaid and Cheney* [1991]:

$$\frac{\partial u}{\partial x}(x) \cong \left(\frac{u_i - u_{i-1}}{x_{i+1} - x_i} \right). \tag{A1}$$

In the geometry of Figure A1, the derivative is the length of line segment PQ divided by the length of line segment QR, or the slope of line segment PR. Derivatives calculated in this manner can be used to estimate the strains and then the stresses [*Chou and Pagano*, 1967].

The spline technique has a key advantage over difference methods in the context of polygonal elements: data points need not be evenly spaced or be on a rectangular grid. For the problem at hand, the points at which displacements are known indeed are not evenly spaced. The irregularly spaced data could be projected onto a rectangular grid, but this has two associated difficulties. First, the use of gridding requires extra computation and will introduce some error. Second, the number of grid nodes needed to adequately represent the displacement field would greatly exceed the number of triangular elements. As a result, the finer grid spacing makes an approach using gridding and finite differences more susceptible to numerical errors than using splines on relatively coarse triangular elements. Our tests indicated that the spline method yielded significantly better results.

Nonetheless, the spline method is susceptible to error. For example, it would not yield a displacement derivative of zero at shaded element in Figure A1 where the displacement is a local maximum. We avoided this problem by generating elements such that their centroids do not fall where derivatives might be expected to equal zero.

There are inherent difficulties in evaluating the displacement derivatives when the displacements are discontinuous between adjacent elements. Imagine trying to evaluate the average slope of

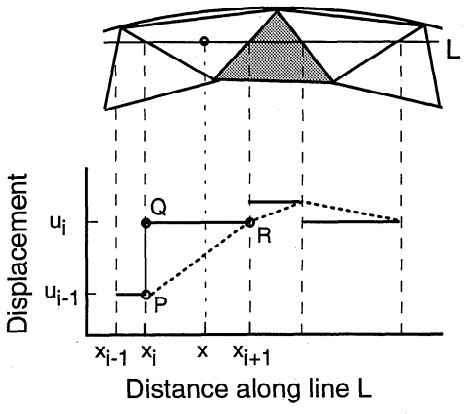

Figure A1. Stepped displacement profile (solid line) along a traverse across part of a fracture defined by triangular elements.

a portion of a spiral staircase from two adjacent steps which might be of different widths. How does tread width affect the slope? How does tread shape affect the slope? At what point along the two steps should the slope be assigned? For the problem at hand, these difficulties were reduced but not eliminated by using smaller elements to define a penny-shaped fracture.

Difficulties also arise because the triangle centroids generally are not aligned along strike or dip; they are staggered. This causes contour graphs of element-face stresses to show regions outlined with fluted or convoluted boundaries. Numerous disconnected "island" contours also can arise, especially where derivatives are near zero. Smaller elements produce smaller amplitude irregularities in contour lines but still tend to produce "islands."

Clearly, there are many potential sources of artifacts in evaluating the derivatives. Some of these artifacts are present in Figure 7, but gross errors appear to be absent. The contour lines near the inner boundary of the cohesive zone show no striking anomalies and cross both the cohesive zone boundary and the adjacent rings of elements smoothly.

Acknowledgments. We thank Jim Evans, Kevin Hestir, Jane Long, Janet Jacobsen, and Michele Cooke for numerous stimulating and constructive discussions associated with this study. Reviews by Richard Schultz, Leonid Germanovich, and an anonymous reviewer contributed to an improved final manuscript. Stephan Bergbauer, Matthew Long, Linda Martel, Owen Martel, and Jordan Muller assisted in the field work. David Pollard graciously provided a copy of the source code for Poly3D. We thank John and Jenise Cunningham of the High Sierra Pack Station for their years of courteous and professional service in support of field work along Bear Creek. We gratefully acknowledge support from the U.S. Department of Energy Office of Basic Energy Sciences (grant DE-FG03-85ER14525) and the Office of Naval Research (grant N00014-86-1-0353). This is SOEST Publication 4636.

References

Adams, M., and G. Sines, Crack extension from flaws in a brittle material subject to compression, *Tectonophysics, 49*, 97-118, 1978.

Ague, J. J., and G. H. Brimhall, Magmatic arc asymmetry and distribution of anomaluous plutonic belts in the batholiths of California: Effects of assimilation, crustal thickness, and depth of crystallization, *Geol. Soc. Am. Bull., 100*, 912-927, 1988.

Barenblatt, G. I., The mathematical theory of equilibrium cracks in brittle fracture, *Adv. Appl. Mech., 7*, 55-129, 1962.

Barnett, J. A. M., J. Mortimer, J. H. Rippon, J. J. Walsh, and J. Watterson, Displacement geometry in the volume containing a single normal fault, *AAPG Bull., 71*, 925-937, 1987.

Brace, W. F., and E. G. Bombolakis, A note on brittle crack growth in compression, *J. Geophys. Res., 68*, 3709-3713, 1963.

Broek, D., *Elementary Fracture Mechanics*, 469 pp., Kluwer Acad., Norwell, Boston, 1983.

Brown, S. R., Fluid flow through rock joints: The effect of surface roughness, *J. Geophys. Res., 92*, 1337-1347, 1987.

Bürgmann, R., and D. D. Pollard, Strain accommodation about strike-slip fault discontinuities in granitic rock under brittle-to-ductile conditions, *J. Struct. Geol., 16*, 1655-1674, 1994.

Bürgmann, R., D. D. Pollard, and S. J. Martel, Slip distributions on faults: Effects of stress gradients, inelastic deformation, heterogeneous host-rock stiffness, and fault interaction, *J. Struct. Geol., 16*, 1675-1690, 1994.

Childs, C., A. Nicol, J. J. Walsh, and J. Watterson, Growth of vertically segmented normal faults, *J. Struct. Geol., 18*, 1389-1397, 1996.

Chou, P. C., and N. J. Pagano, *Elasticity*, 290 pp., D. Van Nostrand, Princeton, N.J., 1967.

Christiansen, P. C., Faulting and hydrothermal processes in a granitic batholith, Ph.D. thesis, Stanford Univ., Stanford, Calif., 1995.

Cladouhos, T. T., and R. Marret, Are fault growth and linkage models consistent with power-law distributions of fault lengths?, *J. Struct. Geol., 18*, 281-293, 1996.

Cooke, M. L., Fracture localization along faults with spatially varying friction, *J. Geophys. Res., 102*, 22,425-22,434, 1997.

Cooke, M. L., and D. D. Pollard, Fracture propagation under mixed mode loading within rectangular blocks of polymethylmethacrylate, *J. Geophys. Res., 101*, 3387-3400, 1996.

Cowie, P. A., and C. H. Scholz, Physical explanation for the displacement-length relationship of faults using a post-yield fracture mechanics model, *J. Struct. Geol., 14*, 1133-1148, 1992.

Cox, S. J. D., and C. H. Scholz, Rupture initiation in shear fracture of rocks: An experimental study, *J. Geophys. Res., 93*, 3307-3320, 1988a.

Cox, S. J. D., and C. H. Scholz, On the formation and growth of faults: An experimental study, *J. Struct. Geol., 10*, 413-430, 1988b.

Crouch, S. L., and A. M. Starfield, *Boundary Element Methods in Solid Mechanics*, 322 pp., Allen and Unwin, Winchester, Mass., 1983.

Cruikshank, K. M., G. Zhao, and A. M. Johnson, Analysis of minor fractures associated with joints and faulted joints, *J. Struct. Geol., 13*, 865-866, 1991.

Dugdale, D. S., Yielding of steel sheets containing slits, *J. Mech. Phys. Solids, 8*, 100-104, 1960.

Erdogan, F., and G. C. Sih, On the crack extension in plates under plane loading and transverse shear, *J. Basic Eng., 85*, 519-527, 1963.

Forster, C. B., and J. P. Evans, Hydrogeology of thrust faults and crystalline thrust sheets: Results of combined field and modeling studies, *Geophys. Res. Lett., 18*, 979-982, 1991.

Germanovich, L. N., R. L. Salganik, A. V. Dyskin, and K. K. Lee, Mechanicsms of brittle fracture of rock with preexisting cracks in compression, *Pure Appl. Geophys., 143*, 117-149, 1994.

Germanovich, L. N., B. J. Carter, A. R. Ingraffea, A. V. Dyskin, and K. K. Lee, Mechanics of 3-D crack growth under compressive loads, in *Rock Mechanics: Tools and Techniques,* edited by M. Aubertin, F. Hassani, and H. Mitri, pp. 1151-1160, A. A. Balkema, Brookfield, Vt., 1996.

Granier, T., Origin, damping, and pattern of development of faults in granite, *Tectonics, 4*, 721-737, 1985.

Hestir, K., S. J. Martel, S. Vail, J. C. S. Long, P. D'Onfro, and W. Rizer, Inverse hydrologic modeling using stochastic growth algorithms, *Water Resour. Res.*, 1998.

Ingraffea, A., Theory of crack initiation and propagation in rock, in *Fracture Mechanics of Rock*, edited by B. K. Atkinson, pp. 71-110, Academic, San Diego, Calif., 1987.

Kanninen, M. F., and C. H. Popelar, *Advanced Fracture Mechanics*, 563 pp., Oxford Univ. Press, New York, 1985.

Kassir, M. K., and G. C. Sih, *Three-Dimensional Crack Problems*, 452 pp., Noordhoof, Leiden, Netherlands, 1975.

Kincaid, D., and W. Cheney, *Numerical Analysis: Mathematics of Scientific Computing*, 690 pp., Brooks/Cole, Pacific Grove, Calif., 1991.

Lawn, B. R., and T. R. Wilshaw, *Fracture of Brittle Solids*, 204 pp., Cambridge Univ. Press, New York, 1975.

Lee, J.-J., and R. L. Bruhn, Structural anisotropy of normal fault surfaces, *J. Struct. Geol., 18*, 1043-1059, 1996.

Lockwood, J. P., and J. G. Moore, Regional deformation of the Sierra Nevada, California, on conjugate microfault sets, *J. Geophys. Res., 84*, 6041-6049, 1979.

Long, J. C. S., and P. A. Witherspoon, The relationship of the degree of interconnection to permeability in fracture networks, *J. Geophys. Res., 90*, 3087-3098, 1985.

Mansfield, C. S., and J. A. Cartwright, High resolution fault displacment mapping from three-dimensional seismic data: Evidence for dip linkage during fault growth, *J. Struct. Geol., 18*, 249-263, 1996.

Martel, S. J., Formation of compound strike-slip fault zones, Mount Abbot quadrangle, California, *J. Struct. Geol., 12*, 869-882, 1990.

Martel, S. J., Effects of cohesive zones on small faults and implications for secondary fracturing and fault trace geometry, *J. Struct. Geol., 19*, 835-847, 1997.

Martel, S. J., and J. P. Evans, Structure of a Sierra Nevada fault zone and hydrologic implications, *Geol. Soc. Am. Abstr. Programs, 28*, A135, 1996.

Martel, S. J., and J. E. Peterson Jr., Interdisciplinary characterization of fracture systems at the US/BK site, Grimsel Laboratory, Switzerland, *Int. J. Rock Mech. Min. Sci. Geomech. Abstr., 28*, 295-323, 1991.

Martel, S. J., and D. D. Pollard, Mechanics of slip and fracture along small faults and simple strike-slip fault zones in granitic rock, *J. Geophys. Res., 94*, 9417-9428, 1989.

Martel, S. J., D. D. Pollard, and P. Segall, Development of simple fault zones in granitic rock, Mount Abbot quadrangle, Sierra Nevada, California, *Geol. Soc. Am. Bull., 100*, 1451-1465, 1988.

Moore, J. G., Geology of the Mount Pinchot quadrangle, southern Sierra Nevada, California, *U.S. Geol. Surv. Bull., 1130*, 152 pp., 1963.

National Academy of Sciences, *Rock Fractures and Fluid Flow:*

Contemporary Understanding and Application, 551 pp., Nat. Res. Counc., Washington, D. C., 1996.

Nicol, A., J. Watterson, J. J. Walsh, and C. Childs, The shapes, major axis orientations and displacement patterns of fault surfaces, *J. Struct. Geol.*, *18*, 235-248, 1996.

Peng, S., and A. M. Johnson, Crack growth and faulting in cylindrical specimens of Chelmsford granite, *Int. J. Rock Mech. Min. Sci. Geomech. Abstr.*, *9*, 37-86, 1972.

Pollard, D. D., and A. Aydin, Progress in understanding jointing over the past century, *Geol. Soc. Am. Bull.*, *100*, 1181-1204, 1988.

Pollard, D. D., and P. Segall, Theoretical displacements and stresses near fractures in rock, in *Fracture Mechanics of Rock*, edited by B. K. Atkinson, pp. 277-349, Academic, San Diego, Calif., 1987.

Pollard, D. D., P. Segall, and P. Delaney, Formation and interpretation of dilatant echelon cracks, *Geol. Soc. Am. Bull.*, *93*, 1291-1303, 1982.

Power, W. L., T. E. Tullis, S. R. Brown, G. N. Boitnot, and C. H. Scholz, 1987, Roughness of natural fault surfaces, *Geophys. Res. Lett.*, *14*, 29-32, 1987.

Rudnicki, J., Fracture mechanics applied to the Earth's crust, *Annu. Rev. Earth Planet. Sci.*, *8*, 489-525, 1980.

Scholz, C. H., *The Mechanics of Earthquakes and Faulting*, 439 pp., Cambridge Univ. Press, New York, 1990.

Segall, P., and D. D. Pollard, Mechanics of discontinuous faults, *J. Geophys. Res.*, *85*, 4337-4350, 1980.

Segall, P., and D. D. Pollard, Nucleation and growth of strike slip faults in granite, *J. Geophys. Res.*, *88*, 555-568, 1983.

Segall, P., and C. Simpson, Nucleation of ductile shear zones on dilatant fractures, *Geology*, *14*, 56-59, 1986.

Segall, P., E. H. McKee, S. J. Martel, and B. D. Turrin, Late Cretaceous age of fractures in the Sierra Nevada batholith, *Geology*, *18*, 1248-1251, 1990.

Sibson, R. H., Structural permeability of fluid-driven fault-fracture meshes, *J. Struct. Geol.*, *18*, 1031-1042, 1996.

Sneddon, I. N., The distribution of stress in the neighborhood of a crack in an elastic solid, *Proc. R. Soc. London, Ser. A*, *187*, 229-260, 1946.

Tada, K., P. C. Paris, and G. R. Irwin, *The Stress Analysis of Cracks Handbook*, Del Res., Hellertown, Pa., 1973.

Tapponier, P., and W. F. Brace, Development of stress induced microcracks in Westerly granite, *Int. J. Rock Mech. Min. Sci. Geomech. Abstr.*, *13*, 103-112, 1976.

Thomas, A. L., Poly3D: A three-dimensional, polygonal element, displacement discontinuity boundary element computer program with applications to fractures, faults, and cavities in the Earth's crust, M.S. thesis, Stanford Univ., Stanford, Calif., 1993.

Thompson, M. E., and S. R. Brown, The effect of anisotropic surface roughness on flow and transport in fractures, *J. Geophys. Res.*, *96*, 21,923-21,932, 1991.

Walsh, J.J., and J. Watterson, Displacement gradients on fault surfaces, *J. Struct. Geol.*, *11*, 307-316, 1989.

Westman, R. A., Asymmetric mixed boundary value problems of the elastic half-space, *J. App. Mech.*, *32*, 411-417, 1965.

Willemse, E. J. M., Segmented normal faults: Correspondence between three-dimensional models and field data, *J. Geophys. Res.*, *102*, 675-692, 1997.

Willemse, E. J. M., D. D. Pollard, and A. Aydin, Three-dimensional analyses of slip distributions on normal fault arrays with consequences for fault scaling, *J. Struct. Geol.*, *18*, 295-309, 1996.

Wong, T.-f., Micromechanics of faulting in Westerly granite, *Int. J. Rock Mech. Min. Sci. Geomech. Abstr.*, *19*, 49-64, 1982.

Wojtal, S.F., Changes in fault displacement populations correlated to linkage between faults, *J. Struct. Geol.*, *18*, 265-279, 1996.

W. Boger and S. J. Martel, Department of Geology and Geophysics, University of Hawaii, 2525 Correa Road, Honolulu, HI 96822. (e-mail: martel@soest.hawaii.edu)

(Received August 4, 1997; revised April 13, 1998;
accepted April 20, 1998.)